PCCP

Parameter Space Exploration Reveals Interesting Mn-doped SrTiO3 Structures

Journal:	*Physical Chemistry Chemical Physics*
Manuscript ID	CP-ART-05-2021-002417.R1
Article Type:	Paper
Date Submitted by the Author:	22-Jul-2021
Complete List of Authors:	Repa, Gil; Lehigh University, Department of Chemisry Fredin, Lisa; Lehigh University, Lisa Fredin;

SCHOLARONE™
Manuscripts

PCCP

ARTICLE TYPE

Parameter Space Exploration Reveals Interesting Mn-doped SrTiO$_3$ Structures†

Gil M. Repa,[a] and Lisa A. Fredin[*a]

The rich chemistry of the SrTiO$_3$ is often modified, intentionally or unintentionally, through the inclusion of defects and dopants. Much computational effort using periodic boundary DFT has been dedicated towards understanding how these observed properties arise from the disordered perovskite structure, but the range of possible defect chemistries arising from different computational modeling choices has not been thoroughly explored. In this study, we calculate the geometric and electronic properties for a systematic range of supercells, from approximately 40 atoms to approximately 320 atoms, with each atomic vacancy and doped with Mn ions to isolate the contribution of supercell size to predicted properties. Our thorough analysis of the electronic and geometric structure of each defected supercell shows high variability, illustrating the need to map such parameter space in order to achieve a comprehensive model of disordered perovskites. Our results additionally reveal fundamental insights into dopant chemistry in SrTiO$_3$, and we report new potential geometric and electronic structures for the Mn-structure that can be used to justify and guide additional experimental investigation into this complex material.

1 Introduction

The perovskite SrTiO$_3$ receives significant scientific attention both as a candidate material for wide ranging applications in photocatalysis[1,2], thermoelectric generation[3], and electronics[4], as well as a model system for understanding the fundamental structural and rich electronic properties of the wider perovskite family[5]. Whether intentional or not, SrTiO$_3$ in experiments is frequently used with defects which have the potential to significantly alter or improve measured properties. In addition to atomic vacancies, the introduction of foreign atoms into the native crystal lattice is a critical means to engineer functionality[6]. Interest in understanding the fundamental consequences of disorder in the perovskite lattice has sparked an explosion of experimental and first principles studies[7–12].

The structure of SrTiO$_3$ lends itself well to computational study by the supercell method in periodic boundary density functional theory (DFT). The bulk form can be considered as a linked network of corner sharing TiO$_6$ octahedra forming a *ccp* array around higher coordination sites for Sr^{2+} cations. Two cubic unit cells can be written for this structure (Fig. S1, ESI†) with one centered on Sr-sites coordinated ionically by 12 O^{2-} anions with corners of Ti atoms (A-cell), and one centered on Ti-sites, coordinated

covalently by six O^{2-} anions with corners of Sr atoms (B-cell). The former case is the intuitive building block for computational supercells. For example, a 2 x 2 x 2 SrTiO$_3$ supercell would imply two A-cells repeated along all three lattice vectors. Despite its relatively simple bulk structure, understanding the complex chemistry of disorder in SrTiO$_3$ continues to present a significant challenge to theoreticians. For example, oxygen vacancies (V_O) in nonstoichiometric SrTiO$_3$ have been associated with a shift in conductivity[13], blue-green light emission[14], and an antiferrodistortive phase transition[15] of the SrTiO$_3$ lattice, yet studies to probe the nature of these behaviors produce contradictory results.

It is well documented that in the case of the V_O, there is extreme sensitivity to supercell size that has confounded attempts to explain the origins of its unique properties. In 2004, Buban and coworkers[16] showed that a 40 atom 2 x 2 x 2 supercell predicted a deep defect state, while larger supercells through the 160 atom 2 x 2 x 4 and 320 atom 4 x 4 x 4 predicted a shallow defect state with primarily t_{2g} character. Similar results were observed with GGA + U methods, where occupied intra-bandgap defect states were observed until blue shifted above the conduction band minimum in even larger 625 and 1080 atom supercells[15]. Such dependence on supercell size was recently confirmed with the extended Hubbard DFT + U + V approach of Ricca et al.[7], and persists even with the use of hybridized functionals HSE06[17,18] and B3PW[19]. Although the dependence on supercell size is well established in this case, the type of defect-defect interactions contributing calculation artifacts, whether quantum mechanical, electro-

[a] *Department of Chemistry, Lehigh University, Bethlehem, PA, 18015, USA. E-mail: laf218@lehigh.edu*
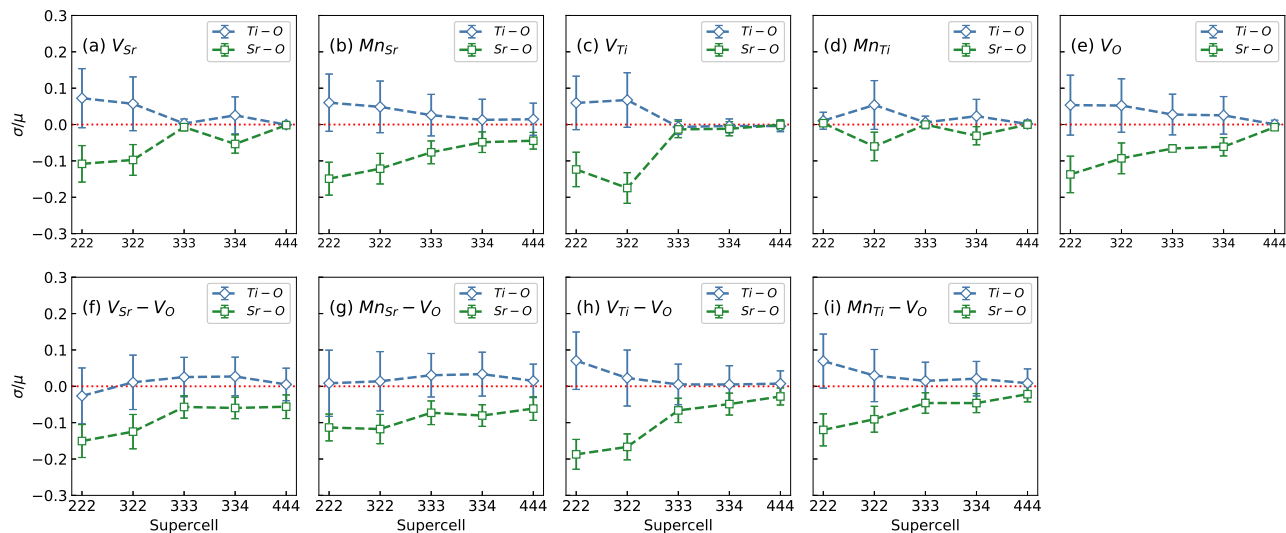
Figu 1 Deviation (σ) and variation (μ) of Ti—O (blue) and Sr—O (green) bond lengths from the pure crystal structure (red) for each unit cell and defect (a-i). A data point above the reference value should be interpreted as elongation of the average bond length, and is reported directly in Å. Error bars are reported with magnitude σ/μ to allow direct comparison of the magnitude of Sr—O and Ti—O variation. For asymmetric 3 × 2 × 2 and 3 × 3 × 4 supercells, only the x- oriented defect is plotted.

static, elastic, or magnetic in nature is often near-impossible to resolve[20].

Despite comparable importance, the same systematic rigor probing the relation between supercell size and V_O defect chemistry is critically lacking for other defect types, including vacancies of Sr and Ti atoms (V_{Sr} and V_{Ti} respectively). Metal vacancies in SrTiO$_3$ are important for controlling both the mechanical and electronic properties of the material, such as grain boundary structure[21] and ionic conductivity[22]. Using 3 x 3 x 3 supercells and a finite size correction scheme, Baker et al.[23] showed that V_{Sr} is the majority defect in SrTiO$_3$, with a much higher formation energy for B-site defects[23]. However, V_{Ti} has been experimentally observed in bulk SrTiO$_3$ by positron annihilation spectroscopy[24,25]. In addition to these two defects, a comprehensive model of realistic SrTiO$_3$ would need to consider two Schottky vacancies, specifically adjacent V_O and metal vacancies (V_{Sr}–V_O, V_{Ti}–V_O), both of which have important implications in applications involving ionic conductivity[22], and for the formation of dopant complexes[26,27].

With regard to supercell size, the situation is further confounded when considering SrTiO$_3$ structures doped with non-native elements, such as Mn^{4+}. These dopants not only produce potentially more complicated defect geometries requiring reorganization of a larger number of atoms, but also have the possibility of magnetic interactions among periodic defect images further introducing artifacts into the calculation. The Mn dopant is of special interest because it is intermediate in size between the Sr and Ti, and its variable oxidation states allow it to substitute for both Sr and Ti atoms (Mn$_{Sr}$ and Mn$_{Ti}$ respectively)[28,29]. Properties can be further tuned by controlling oxygen concentration and forming the analogous double defects (Mn$_{Sr}$–V_O, Mn$_{Ti}$–V_O)[30,31]. Like metal vacancies, doped supercells require careful investigation to understand results that are simply an artifact of model

choice and which provide much needed understanding of this important material.

Here the first systematic and comprehensive study of the relation between calculated properties of SrTiO$_3$ point defects and supercell size is presented. By focusing on a thorough analysis of both the geometric and electronic properties of each defect, the disappearance of defect-defect interactions and bulk behavior in the dilute range will emerge as supercell size increases. It should be noted that extrapolation of a supercell that is "big enough" for one defect type to another defect type is a hazardous approach as the types of interactions contributing artifacts may be highly variable. Furthermore, with computational studies providing a much higher resolution than current experimental techniques, there is no standard for comparison, and thus the only way to identify such computational artifacts is through thorough systematic benchmarking like the one presented here.

2 Computational Methods

In order to probe the relationship between model parameters and calculated properties, we performed DFT calculations on a systematic range of five differently sized supercells varying from a small 40 atom supercell in which the perovskite A-cell is repeated two times along each lattice vector, to a large 320 atom supercell with four repeats of the A-cell. We refer to each of these supercells in increasing size as 2 x 2 x 2 (40 atoms), 3 x 2 x 2 (60 atoms), 3 x 3 x 3 (135 atoms), 3 x 3 x 4 (180 atoms), and 4 x 4 x 4 (320 atoms) to denote the number of A-cell repeats along the *x-*, *y-*, and *z*-axes respectively. For each supercell, we considered the following vacancies and Mn^{4+} dopants: $(V_{Sr})^{2-}$, $(V_{Ti})^{4-}$, $(V_O)^{2+}$, $(V_{Sr}$–$V_O)^0$, $(V_{Ti}$–$V_O)^{2-}$, $(Mn_{Sr})^{2+}$, $(Mn_{Ti})^0$, $(Mn_{Sr}$–$V_O)^{4+}$, and $(Mn_{Ti}$–$V_O)^{2+}$. Additionally, the asymmetric 3 x 2 x 2 and 3 x 3 x 4 supercells possess additional defects with two nonequivalent sites for V_O and different distances between periodic defect images, notated as $-V_{Ox}$ and $-V_{Oz}$ to indicate the orientation. We also tested
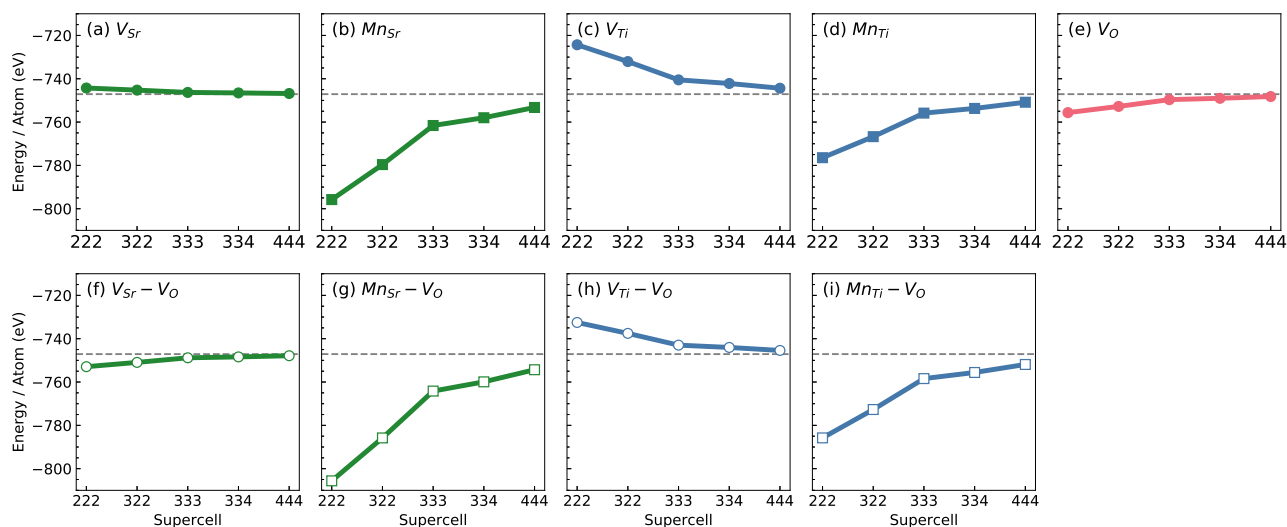
Figu 2 Normalized energy per atom for each defect and super cell (a-i). The gray line represents energy of the pure supercells which is relatively invariant. For asymmetric 3 × 2 × 2 and 3 × 3 × 4 supercells, only the x- oriented defect is plotted.

the dependence on supercell net charge and dopant valence by considering the Mn-doped 3 x 3 x 3 supercells with an additional one or two electrons to simulate doping with Mn^{3+} and Mn^{2+} respectively. In total, we calculated energetics, optimized geometry, and electronic structure of 70 different supercells.

Fixed volume geometry optimizations were carried out using the QuantumEspresso package[32,33] and a 600 eV cutoff for the planewave basis set with Γ-point sampling of the Brillouin zone. Electron exchange and correlation were accounted for under the generalized gradient approximation (GGA) with the Becke-Lee-Yang-Parr (BLYP) functional[34,35], which is comparable to literature investigations using PBE and PBEsol[36,37]. Full band structures of each were calculated with the same conditions and an expanded k-point mesh (Table S1, ESI†). Under this computational setup, calculation of full bands for the largest Mn-doped 3 x 3 x 4 and 4 x 4 x 4 supercells were prohibitively expensive. To confirm the quality of our BLYP-calculated electronic structures, we also performed band calculations of each supercell with the projector-augmented wave (PAW) method in the Vienna Ab Initio Simulation Package (VASP)[38–40] and the hybrid HSE06 functional[41,42] with Γ-only sampling and same 600 eV energy cutoff. The following core/valence configurations were used for each element: Sr:[Ar]3d/4s4p5s, Ti:[Ne]3s/3p4s3d, O:[He]/2s2p, Mn:[Ne]3s/3p4s3d.

3 Results and Discussion

A detailed analysis of geometry and energetics with respect to supercell size reveals that caution must be taken when designing computational models of defected materials. Different supercell sizes inherently represent different chemistries and defect densities, thus providing varying and potentially unphysical predictions. Computation is always a tradeoff between accuracy and computational cost. In particular, calculations involving supercells with hundreds of atoms are computationally demanding to optimize. The wall time, reported as total core-hours, for BLYP

geometry optimizations (Fig. S2, ESI†) and HSE06 single point calculations (Fig. S3, ESI†) of each defected supercell demonstrates an exponential increase in computational cost when moving to larger cell sizes. Table S2 (ESI†) demonstrates this scaling on a per-atom basis for both calculations.

3.1 Supercells vs Bulk Geometric Structure

In perovskite oxides the tuning of the dopant location based on changing synthetic parameters before dopant loading[28] indicates that doped structures are highly dependent on the locations of as synthesized vacancies in the material. To understand the formation of such vacancies, we optimized all possible single atom vacancies, V_{Ti}, V_{Sr}, and V_O.

Generally, structural distortions are largest for the smaller supercells, and converge to the bulk $SrTiO_3$ structure as the number of atoms in the supercell increases. Structural deviation is quantified for each supercell and defect type by comparing the average adjusted mean Sr–O and Ti–O bond lengths (Fig. 1a-i). In almost all supercells, optimization decreases the average Sr–O bond length (μ) and increases the average Ti–O bond length. The nature of the convergence to bulk structure reveals three different patterns of cell-wide structural distortion: (i) asymmetric supercells can result in increased distortion, best illustrated by considering the Mn_{Ti} defect (Fig. 1d). (ii) A number of defects studied here are capable of inducing cell-wide antiferrodistortive-like rotations of Ti-O octahedra. We calculate these out-of-phase rotations to be $\theta \approx 1.0°$ around the b-axis in the 4 x 4 x 4 $V_{Sr}–V_O$ supercell (Fig. S7). Such rotations are largely driven by geometric constraints[43] with experimental measurement of strained undoped $SrTiO_3$ at $\theta = 2.01°$ at 50 K[44]. Further distortion of these octahedra occurs from off-centering of the central Ti atoms. This reduces the symmetry of each octahedra from O_h to C_{3v} and results in a bimodal distribution of Ti-O bondlengths around the pure value for a large number of supercells (Fig. S8-S11). This second symmetry-lowering effect likely arises from electronic in-
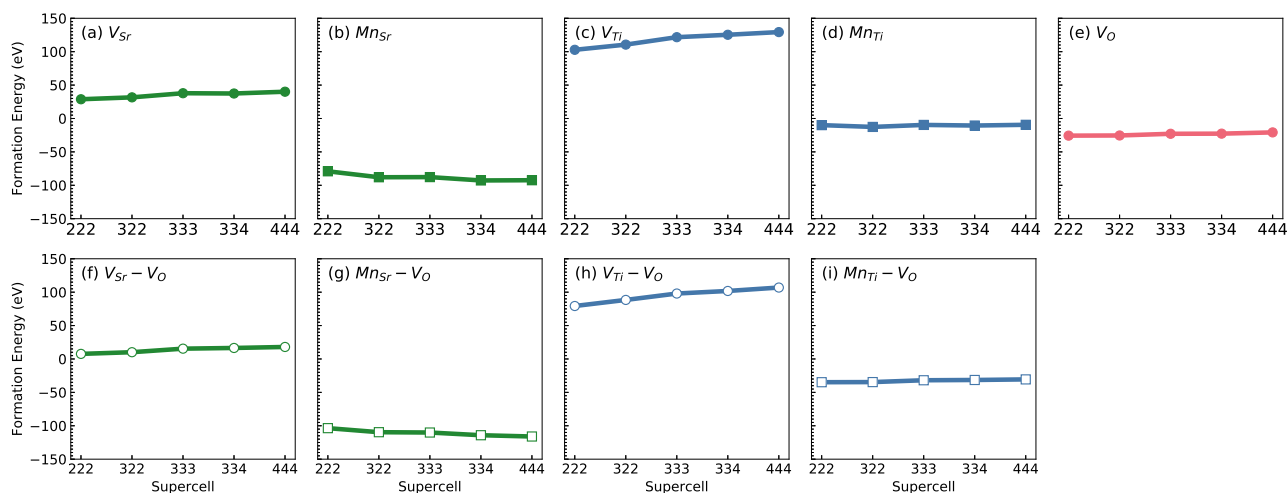
Figu 3 Formation energy for each defected supercell (a-i). For asymmetric 3 × 2 × 2 and 3 × 3 × 4 supercells, only the x- oriented defect is plotted.

stabilities of the Ti atom[45], and explains the unique shapes of Ti-O deviation for V_{Sr}–V_O and Mn_{Sr}–V_O (Fig. 1f & 1g). (iii) The periodic boundary conditions of 2 x 2 x 2 and 3 x 2 x 2 supercells can induce unusually high structural distortion. This is best illustrated in the case of V_{Ti} (Fig. 1c), where the bulk structure is dramatically achieved at the 3 x 3 x 3 supercell. The high distortion in the smallest supercells arises from the high density of defects, and boundary-spanning reorganizations that may introduce nonphysical artifacts into calculated geometries.

Analyzing the energy per atom for each supercell further shows exceptionally high deviation from the bulk value for defected supercells smaller than 3 x 3 x 3 (Fig. 2 & Table S3, ESI†). In the undefected supercells, the energy per atom is invariant at 747 eV/atom (Table S3, ESI†). Defected supercells converge towards this value nonlinearly as the size of the supercell increases. In the case of V_{Sr} and V_{Sr}–V_O (Fig. 2a & 2f), this effect is minimal as the energy slightly decreases or increases to the reference value respectively. This small deviation is possibly attributed to the highly electropositive nature of Sr, whereas disruption of the covalent Ti-O cubic lattice results in much larger deviation from bulk value in V_{Ti} and V_{Ti}–V_O supercells (Fig. 2c & 2h). The largest deviation occurs for the Mn-doped supercells which always increase to the reference value (Fig. 2b, 2d, 2g & 2i).

The formation energy is less dependent on unit cell size than energy per atom, and generally shows a marginal increase with increasing cell size (Fig. 3 & Table S4, ESI†). We calculate formation energy according to the formula:

$$E_{form} = E_{doped} - E_{pure} + E_x - E_{Mn}$$

Where E_{doped} and E_{pure} are the final BLYP energies of each optimized supercell, and E_x and E_{Mn} are the energies of the defect and dopant atoms in an empty vacuum cell of respective size. Both single metal vacancies result in endothermic formation energies with the largest occurring for V_{Ti} in excess of 100 eV (Fig. 3c). Exclusion of an adjacent oxygen vacancy to form the V_{Ti}–V_O defect lowers this value slightly (Fig. 3h), and subsequent doping to Mn_{Ti}–V_O brings exothermic formation energy to approx-
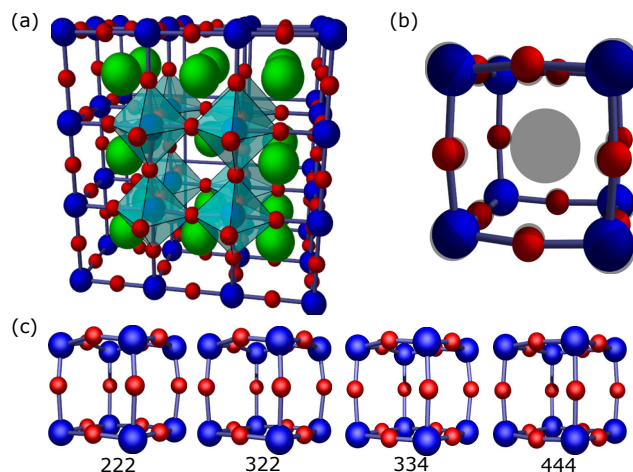
Figu 4 Cutaway of 3 × 3 × 3 V_{Sr} supercell with defect surrounding TiO_6 octahedra (a), and enlarged defected A-cell from 3 × 3 × 3 supercell with locations of atoms in the pure lattice shaded (b). Defected A-cells from each differently sized supercells (c). Color code: Sr = green, Ti = blue, O = red.
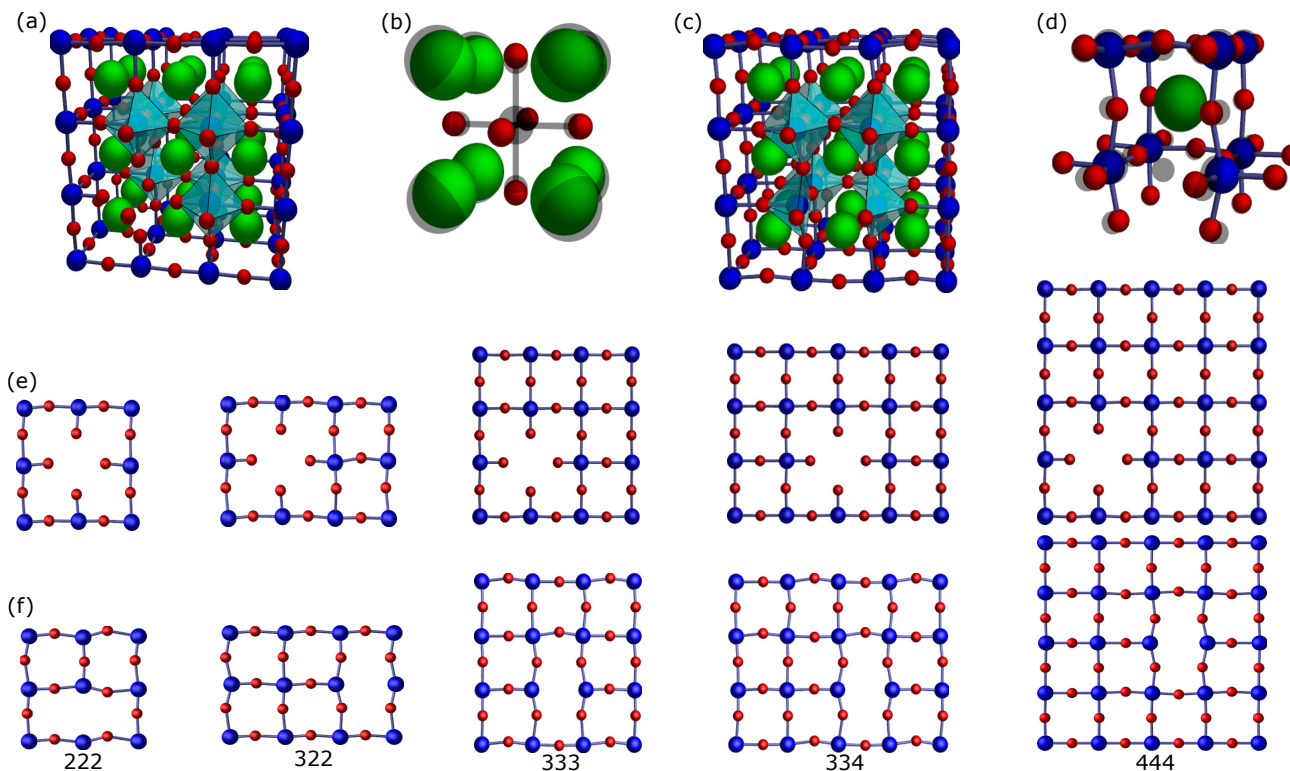
Figu 5 Cutaway of $3 \times 3 \times 3$ V_{Ti} (a) and V_O (c) supercells with defect surrounding TiO_6 octahedra. Enlarged V_{Ti} B-cell (b) and enlarged V_O A-cell (d) from $3 \times 3 \times 3$ supercell with locations of atoms in the pure lattice shaded. Cubic lattice in the defect plane from the V_{Ti} (e) and V_{Ti}-V_O (f) for each differently sized supercell. For asymmetric $3 \times 2 \times 2$ and $3 \times 3 \times 4$ supercells, only the x- oriented defect is shown. Color code: Sr = green, Ti = blue, O = red.

imately -10 eV in the 3 x 3 x 3 supercell (Fig. 3i). A similar trend occurs for A-site defects with formation energy greatest for the endothermic single atom vacancy V_{Sr} (Fig. 3a) and most favorable formation energies occurring for the highly exothermic Mn-doped double defect, Mn_{Sr}–V_O (Fig. 3g). Exothermic formation energies are predicted for the V_O defect (Fig. 3e), and there is no apparent dependence on orientation of the defect (Table S4, ESI†). The lower formation energies of A-site defects than B-site defects have been seen previously[23]. Interestingly, vacancy of the nearest neighbor oxygen site stabilizes both metal site vacancies.

Based on the structure, energy per atom, and formation energies, the 3 x 3 x 3 supercell is ideal for modeling the chemistry of vacancies and Mn-dopants in $SrTiO_3$. By balancing computational expense with an accurate description of structure, the 3 x 3 x 3 supercell critically does not suffer from the ambiguous periodic boundary conditions of the 2 x 2 x 2 and 3 x 2 x 2 supercells. This hypothesis is tested by next considering the specific geometry of each defected cell.

3.2 Geometry of Single Defect Sites
Geometry of the V_{Sr} defect site (Fig. 4) indicates minimal reorganization of the defect-adjacent atoms with the surrounding TiO_6 octahedra remaining largely in their native orientation (Fig. 4a). Extracting the nearest neighbors to the vacancy from the 3 x 3 x 3 supercell in Fig. 4b (*i.e.* the defected A-cell) shows a slight movement of neighboring atoms around the vacancy, with each of the O atoms bowing slightly outwards and Ti atoms moving inwards

toward the defect (gray atoms in Fig. 4b show the bulk atom locations). This same defect site geometry appears to be predicted by all supercells (defect separation from 7.89 – 15.78 Å, Fig. 4c), similarly to the reported V_{Sr}^{2+} geometries[17]. Quantitative analysis of the defect geometry achieved by calculating the volume of a convex hull constructed from the defect adjacent atoms (Fig. 6a) and measuring displacement of nearest neighbor atoms (Fig. 6d), reveals slight deviation between each supercell. We calculate the nearest neighbor displacement[8] as:

$$\langle \delta_{NN_x} \rangle = \frac{1}{N} \sum \delta_i$$

Where x and N are the type and number of atoms considered, and δ_i is the displacement of each atom from its starting position in the pure crystal lattice. Specifically in V_{Sr}, we observe an increase in the reorganization of the defect adjacent Ti atoms ($\langle \delta_{NN_{Ti}} \rangle$, blue line in Fig. 6e) in the 2 x 2 x 2 and 3 x 2 x 2 supercells resulting in a slightly larger defect volume of approximately 4 Å^3.

The 3 x 3 x 3 supercell predicts comparable results for V_{Ti} with the surrounding octahedra remaining intact (Fig. 5a) and the defected B-cell (Fig. 5b) showing neighboring Sr atoms shifting inward towards the vacancy site and O atoms moving directly towards their bonded Ti partners. Aside from this small reduction in Ti–O bond lengths, the cubic lattice remains free from significant distortion in the supercells 3 x 3 x 3 and larger (Fig. 5e), matching previously observed results[17]. Contrarily, the optimized 3 x 2 x 2 and 2 x 2 x 2 supercells predict significantly more out

of plane restructuring. While Fig. 6e indicates Sr reorganization to be the primary contribution to nearest neighbor displacements, the large restructuring seen in the 2 x 2 x 2 and 3 x 2 x 2 is driven by periodic boundary condition-induced destabilization. In these supercells, a significant percentage of Ti atoms are bound two negatively charged defect adjacent O atoms, straining the TiO_6 octahedra. During optimization, defect adjacent O atoms no longer migrate exclusively along one lattice vector directly towards their bonding partner as in Fig. 5b, but rather in multiple dimensions causing the observed distortions. Because the nearest neighbors plot (Fig. 6e) only accounts for displacement and not directionality, this effect is not readily apparent. These differences in calculated geometry underscore the necessity of selecting a large enough supercell for simulation of defects in cubic perovskites.

Analysis of V_O (Fig. 5c) shows that each of the four nearest neighboring O atoms bonded to the undercoordinated Ti atom move inwards towards the defect (Fig. 5d & 5f), while the remaining O atoms comprising the rest of the defected A-cell and bonded parallel to the vacancy bend outward. Similarly, the undercoordinated Ti atoms move slightly outward away from the defect while the neighboring Sr remains in its native position (Fig. 5d). The tetrahedral geometry of the undercoordinated Ti atom results in significant octahedral tilt (Fig. 5c). This geometry is generally well-captured by each of the supercells (Fig. 5f), and matches the geometries calculated by Zhang et al[13]. Interestingly, the outward motion of parallel bonded O atoms is repressed in supercells 2 x 2 x 2 and 3 x 2 x 2, due to the opposing forces arising from periodic boundary conditions. This is well reflected in defect volume and nearest neighbor displacements (Fig. 6c & 6f), which are fairly constant.

3.3 Geometry of Double Defects

Experimental structures of Mn-dopants next to oxygen vacancies have been observed[27,28]. If these structure arise from filling a metal vacancy site that is already next to an oxygen vacancy, then the energetics and geometries of the double defects consisting of a vacancy of both a metal atom and adjacent oxygen are critical. Here, we consider only the nearest neighbor double defect, which results in a defect separation of $\approx 6 - 14$Å.

The 3 x 3 x 3 V_{Sr}–V_O defect cell displays the characteristics of the two corresponding single defects. Those O atoms bonded to the undercoordinated Ti atoms and comprising the neighboring Sr-occupied A-cells are pulled inward (Fig. 7b & 7e), just as before in the V_O defect geometry (Fig. 5). Similarly, the undercoordinated Ti atoms also move away from the defect site. The remaining defect adjacent Ti and O atoms comprising the vacant A-cell are characteristic of the V_{Sr} defect geometry with oxygen atoms buckling outward from the defect site, and slight migration of Ti atoms inward. Analysis of supercells smaller than 3 x 3 x 3 is confounded by the large structural distortion caused by the high defect density and periodic boundary condition induced reorganization. Notably, the 3 x 2 x 2 V_{Sr}–V_O supercell fails to capture the V_{Sr} defect geometry component (Fig. 7e), instead predicting the geometry of a single V_O defect where all O atoms adjacent to the

defect and bonding with the undercoordinated Ti move inwards, losing the outward buckling observed in V_{Sr} defected cells. The high degree of reorganization and unique geometries predicted by the 2 x 2 x 2 and 3 x 2 x 2 supercell account for an unusually high nearest neighbor displacement contributed by large reorganization of O atoms (Fig. 8b).

The V_{Ti}–V_O defect is also best viewed as a composition of two single defect geometries. The five singly bonded oxygens neighboring the Ti vacancy in the defected B-cell (Fig. 7c) migrate towards their sole bonding partners as in the singly defected V_{Ti} cells. Four of these O atoms closest to double vacancy move additionally towards the vacant O site. The four Sr atoms nearest the vacant B site migrate significantly inwards towards the vacancy, while the Sr atoms adjacent to the oxygen vacancy are relatively fixed in their native lattice positions. Those O atoms opposite the Ti vacancy and bound to the undercoordinated Ti move inward forming a tetrahedral geometry (Fig. 7f) as in the V_O supercells. In supercells 3 x 3 x 3 and larger, this inward movement results in tilting the adjacent TiO_6 octahedra with O atoms bonded parallel to the vacant O site moving outwards away from the defect (Fig. 7c & 7f). However, in 2 x 2 x 2 and 3 x 2 x 2 V_{Ti}–V_{Ox}, this octahedral tilt is largely repressed. To achieve the same geometry of the optimized 3 x 3 x 3 supercell under the equivalence of atoms imposed by the periodic boundary conditions of these smaller cells, a single TiO_6 octahedra would have to simultaneously rotate clockwise and counter-clockwise. These two opposing forces result in very little net movement, and a subsequent failure to describe the bonding of these atoms and their relaxation around the vacancy. Notably, the 3 x 2 x 2 V_{Ti}–V_{Oz} (Fig. S8, ESI†) defect is successful in capturing this reorganization as tilt occurs along its lattice vector with period 3, eliminating equivalence restrictions.

The effect of periodic boundary conditions on the optimized geometry is also clearly visible in the nearest neighbor displacements (Fig. 8d). For the two smallest supercells, the reorganization of Sr and O atoms are the major contributors to nearest neighbor displacements with the contribution of Ti atoms negligible. At the 3 x 3 x 3 supercell, Sr displacement is reduced and O displacement is increased to become the major contributor. In the two smallest supercells, the Ti–O cubic lattice is more rigid due the opposing forces created by periodic boundary conditions as previously discussed, justifying the increase in O reorganization at the 3 x 3 x 3 supercell. Similarly, O vacancies in the cubic lattice are stabilized by increased interactions with the Sr atoms evidenced by migration of oxygens around a vacancy towards the Sr atoms in V_O defects. With the periodic boundary-imposed rigidity in the cubic lattice, the Sr–O stabilization interaction is able to overcome the mass difference between Sr and O atoms, and subsequently the Sr atom is pulled, justifying the increased Sr displacement (Fig. 8d).

3.4 Geometry of Dopants

Optimized geometries of an Mn^{4+} ion substituting for Sr show occupation of an off-center lattice position in agreement with previous studies[29,31,46,47]. In the cubic supercells, the Mn ion migrates along all three lattice vectors to a corner of the defected
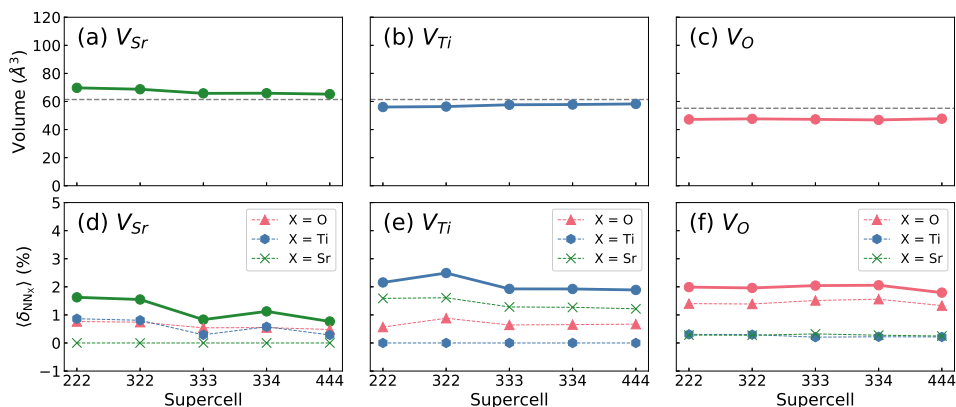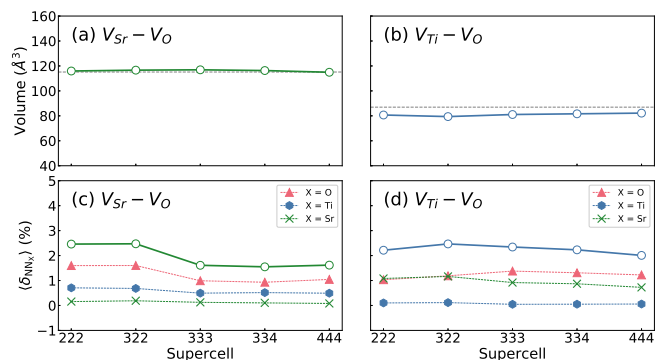
Figu 6 Defect Volumes (a-c) and Nearest Neighbor (d-f) displacements for single vacancies. Defect volumes are approximated by a convex hull constructed from the nearest 20 lattice atoms for V_{Sr} defects and nearest 14 lattice atoms for V_{Ti} and V_O defects. Nearest neighbor migrations are calculated as displacement of these same lattice atoms from the pure crystal structure. The solid line in nearest neighbor plots represents total displacement, while the green, blue, and red dashed lines represent the atom-resolved displacements. For asymmetric supercells, only the x-oriented defect structure is plotted.
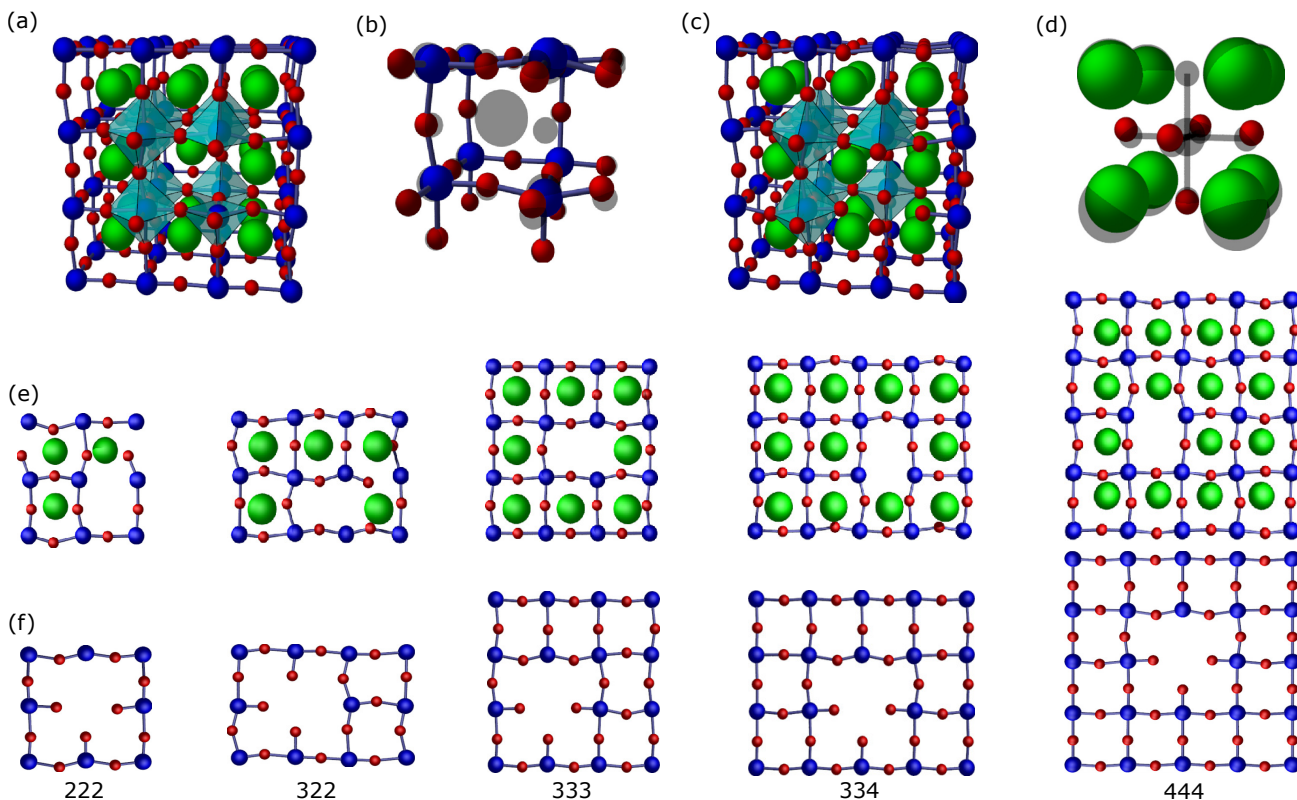
Figu 7 Cutaway of 3 × 3 × 3 V_{Sr}−V_O (a) and V_{Ti}−V_O (c) supercells with defect surrounding TiO$_6$ octahedra. Enlarged V_{Sr}−V_O A-cell (b) and enlarged V_{Ti}−V_O B-cell (d) from 3 × 3 × 3 supercell with locations of atoms in the pure lattice shaded. Cubic lattice in the defect plane from the V_{Sr}−V_O (e) and V_{Ti}−V_O (f) for each differently sized supercell. For asymmetric 3 × 2 × 2 and 3 × 3 × 4 supercells, only the x- oriented defect is shown. Color code: Sr = green, Ti = blue, O = red.

Figu 8 Defect Volumes (a-c) and Nearest Neighbor (d-f) displacements for double vacancies. Defect volumes are approximated by a convex hull constructed from the nearest 26 lattice atoms for V_{Sr}–V_O defects and nearest 18 lattice atoms for V_{Ti}–V_O defects. Nearest neighbor migrations are calculated as displacement of these same lattice atoms. For asymmetric supercells, only the x-oriented defected structure is plotted.

Figu 9 Cutaway of $3 \times 3 \times 3$ Mn$_{Sr}$ supercell with defect surrounding TiO$_6$ octahedra (a), and enlarged defected A-cell with locations of atoms in the pure lattice shaded (b). Defected A-cells from each differently sized supercells (c). Color code: Sr = green, Ti = blue, O = red, Mn = purple.

A-cell (Fig. 9b). Here, the nearest Ti atom is displaced from the center of its octahedra (Fig. 9a), leaving three O atoms to triply coordinate the Mn ion. Those Ti atoms sharing bonding partners with the Mn ion are displaced away, while the remaining four Ti atoms are pulled inwards. With the exception of those lattice ions directly interacting with dopant, the geometry predicted by the cubic supercells is similar to that of V_{Sr}. Notably, the Mn$_{Sr}$ defect is sensitive to the symmetry of the supercell, with a critically different defect geometry predicted for the asymmetric super cells (Fig. 9c). In each case, the Mn ion continues to occupy an off-center lattice position, yet reorganization of the dopant ion only occurs in the lattice vector for which the supercell has the greatest period. In the case of the 3 x 2 x 2 and 3 x 3 x 4 supercells, there is minimal change in the yz- and xy-coordinates of the Mn ion respectively. Consequently, a 4-coordinate face-centered defect complex is formed (coordination number[48] approximately 4.6 (Table S6, ESI†). Because the dopant no longer approaches a B-site ion in this defect geometry, all Ti atoms remain centered in their octahedra, as indicated by the reduced nearest neighbor displacement for Ti in asymmetric supercells (Fig. 12e). However, the implication of four O atoms in formation of the face-centered complex contribute to an increase in the total nearest neighbor displacements for asymmetric supercells. Doping the 3 x 3 x 3 supercell with aliovalent Mn^{2+} and Mn^{3+} ions each predict a distinct 5-coordinate Mn complex (coordination numbers approximately 4.8 and 4.4 respectively, Table S6 and Fig. S13, ESI†) where the dopant moves along two lattice vectors to the edge of a supercell, to produce a square pyramidal dopant complex not captured by any of the Mn^{4+}$_{Sr}$ supercells.

Importantly, while the Mn location in the supercells varies widely, the coordination numbers (Table S6, ESI†) are all in the 4.4–4.8 range. It would be interesting to see if X-ray absorption spectroscopies (XAS) pre-edge features, which indicate the degree of disorder within polyhedra, could be used to determine if there is one clear Mn structure. While measurements like high energy x-ray scattering pair distribution function (PDF) might have this level of resolution for bulk samples, it would be inter-
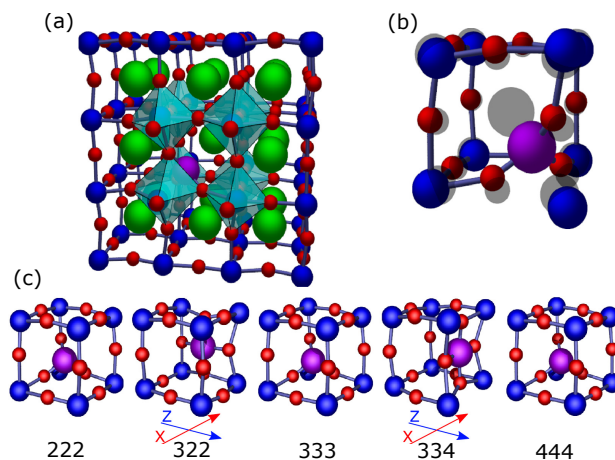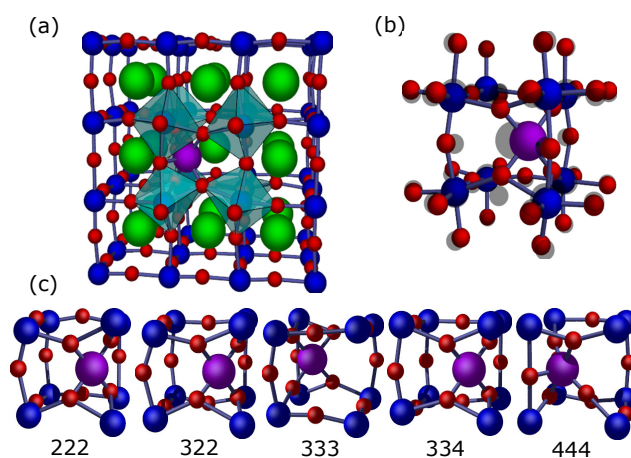
Figu 10 Cutaway of $3 \times 3 \times 3$ Mn$_{Sr}$–V_O supercell with defect surrounding TiO$_6$ octahedra (a), and enlarged defected A-cell with locations of atoms in the pure lattice shaded (b). Defected A-cells from each differently sized supercells (c). For asymmetric supercells, only the x-orientated defect is shown. Color code: Sr = green, Ti = blue, O = red, Mn = purple.

esting to see if anything can be determined experimentally about dopant geometries. Without such evidence, one must assume that a range of Mn structures exist in real materials and thus must be modeled to capture the range of possible electronic effects.

The geometry of the $Mn_{Sr}–V_O$ defect is also sensitive to the supercell size varying with the location of the off-center Mn ion (Fig. 10c). In each case, the Mn dopant reorganizes along 2 lattice vectors causing significant octahedral tilt as it coordinates with O atoms (Fig. 10a). For the 2 x 2 x 2, 3 x 2 x 2, and 3 x 3 x 4 supercells (Fig. 10c), the Mn is positioned directly towards the oxygen vacancy and forms a 4-coordinate Mn complex, distinct from the face-centered Mn complex calculated for the asymmetric Mn_{Sr} defected cells. The 4-coordinate Mn complex is not sensitive to the orientation of the oxygen vacancy in the asymmetric supercells with similar structures predicted for both orientations. A significantly different defect geometry is calculated for the 3 x 3 x 3 and 4 x 4 x 4 supercells, both forming a 5-coordinate Mn complex. However, these supercells differ from each other with the Mn ion moving directly away from (Fig. 10b) or parallel to (Fig. 10c) the O vacancy respectively. Doping the 3 x 3 x 3 supercell with aliovalent Mn^{2+} or Mn^{3+} removes this effect (Fig. S9, ESI†) and reveals the 4-coordinate Mn complex like those predicted by the 2 x 2 x 2, 3 x 2 x 2, and 3 x 3 x 4 $Mn_{Sr}^{4+}–V_O$ structures. Despite the dramatic difference between the different $Mn_{Sr}–V_O$ defect geometries, the nearest neighbor displacement is relatively constant (Fig. 12f). In each case, reorganization of adjacent O atoms is the major contributor, with marginal contributions by Sr and Ti atoms. However, the different defect geometries are detectable by volume (Fig. 12b), with the five coordinate Mn complex formed in 3 x 3 x 3 and 4 x 4 x 4 supercells approximately 10 Å^3 smaller than the 2 x 2 x 2 and 3 x 2 x 2 supercells.

Unlike the dramatic variation and distortion of the $Mn_{Sr}–V_O$, Mn_{Ti} defected supercells show minimum disruption of the native crystal structure (Fig. 11a), probably as the Mn^{4+} ion is similar in size to the substituted Ti. In all supercells, defect adjacent O atoms are pulled towards the substituting Mn ion (Fig. 11e), reducing the neighboring bond lengths in the cubic lattice from 1.97 Å to approximately 1.82 Å. Unlike in the singly defected V_{Ti} supercells, the Sr atoms comprising the B-cell are relatively fixed in cubic supercells (Fig. 11b). Notably, there is increased reorganization of the Sr atoms for the asymmetric supercells indicated by the nearest neighbor displacements (Fig. 12g), a phenomenon which may coincide with the cell-wide folding previously discussed. Geometry optimizations of 3 x 3 x 3 supercells with Mn^{2+} and Mn^{3+} as dopant ions optimize to a similar geometry as their Mn^{4+} doped counterparts (Fig. S9, ESI†) to a comparable Mn–O bond length of 1.83 Å in both oxidation states.

Like the $Mn_{Sr}–V_O$ defect, optimization of $Mn_{Ti}–V_O$ defected supercells also reveals varying defect geometries dependent on supercell size. In all supercells, those O atoms adjacent to the vacancy move inward (Fig. 11f), similar to the reorganization of the V_O defect (Fig. 5), and those bonded to the dopant ion experience the bond length shortening characteristic of the Mn_{Ti} defect (Fig. 11). However, in some of the supercells, reorganization of certain O atoms adjacent to the vacancy and bound to the dopant ion (henceforth referred to as neighboring O atoms)

is much greater resulting two inequivalent Mn–O bond lengths of 1.67 Å and 1.89 Å as measured in the 3 x 3 x 3 supercell. As a consequence, O atoms closer to the Mn ion are no longer equivalent to the remaining neighboring O atoms, and are out of bonding distance with their Ti partners, whose subsequent reorganization further increases the distance between the two atoms to 2.48 Å. Of the 4 neighboring O atoms, inequivalence of this type arises for two (one shown in (Fig. 11f) and is only observed in supercells 2 x 2 x 2, 3 x 2 x 2, 3 x 3 x 3, and 3 x 3 x 4 (–V_{Ox} direction only)). This subtle difference in geometry is not detectable by the nearest neighbor displacement or volume measures (Fig. 12d & 12h). The fact that this effect is diminished for the long 3 x 3 x 4 V_{Oz} and 4 x 4 x 4 supercells indicates that the appearance of these inequivalent neighboring O atoms might just be an artifact of close packing of the defects or defect-defect interactions in the periodic structure. Interestingly, doping with Mn^{2+} reduces the inequivalence of Mn—O bond lengths to 1.76 and 1.84 Å, and inequivalence is completely diminished with Mn^{3+} where all vacancy adjacent Mn–O bond lengths at 1.78 Å.

3.5 Electronic Structure of Undefected and V_O Supercells

The effect of supercell size on calculated electronic properties is readily apparent even in the undefected supercells. Generally, the Γ-only HSE06 calculated bands (Fig. 13a) align well with the full band structures and density of states (DOS) calculated with the BLYP functional (Fig. S10, ESI†). Both functionals confirm the valence band (VB) to have mainly oxygen $2p$ character, and the conduction band (CB) primarily contributed by Ti t_{2g} orbitals. The full band structures show conduction band minima (CBM) occuring at points Γ and X, while location of the valence band maximum (VBM) varies for each supercell. This variation is due in part to differing atomic species at the same high symmetry point in different supercell sizes (Table S7, ESI†). In supercells with an even period in all three lattice vectors, each high symmetry point is centered on a Ti atom, contributing VBM at points X and Γ. In the 3 x 3 x 3 supercell, X and Γ correspond to minima of the valence band, and coincide with an A-cell face center and Sr atom respectively, whereas VBM in these supercells correspond to Ti and O atoms at points M and R. In the BLYP predicted band structures, the magnitude of the band gap (E_g) in pure supercells very consistent at approximately 1.85 eV. However, the hybrid HSE06 functional predicts a much larger E_g with higher variation ranging from a minimum of 2.92 eV in the 2 x 2 x 2 supercell to a maximum of 3.51 eV in the 3 x 3 x 3 supercell. The larger supercells are within computational error of the experimental E_g (3.2 eV, direct 3.7 eV)[49]. We suspect the maximum E_g occurs in the 3 x 3 x 3 supercell as a result of the Γ point sampling, which is centered on a Sr-atom for only the 3 x 3 x 3 supercell.

V_O leads to a large increase in the magnitude of E_g predicted by both the HSE06 (Fig. 13b) and BLYP (Fig. S10, ESI†) functional. In the full BLYP band structures, E_g is increased to a maximum of about 2.70 eV in the 2 x 2 x 2 supercell, gradually converging to bulk value in the large 4 x 4 x 4 supercell. The HSE06 predicted E_g also decreases as supercell size is increased.Other reports have shown a narrowing of E_g[17,18]. There is limited dependence on
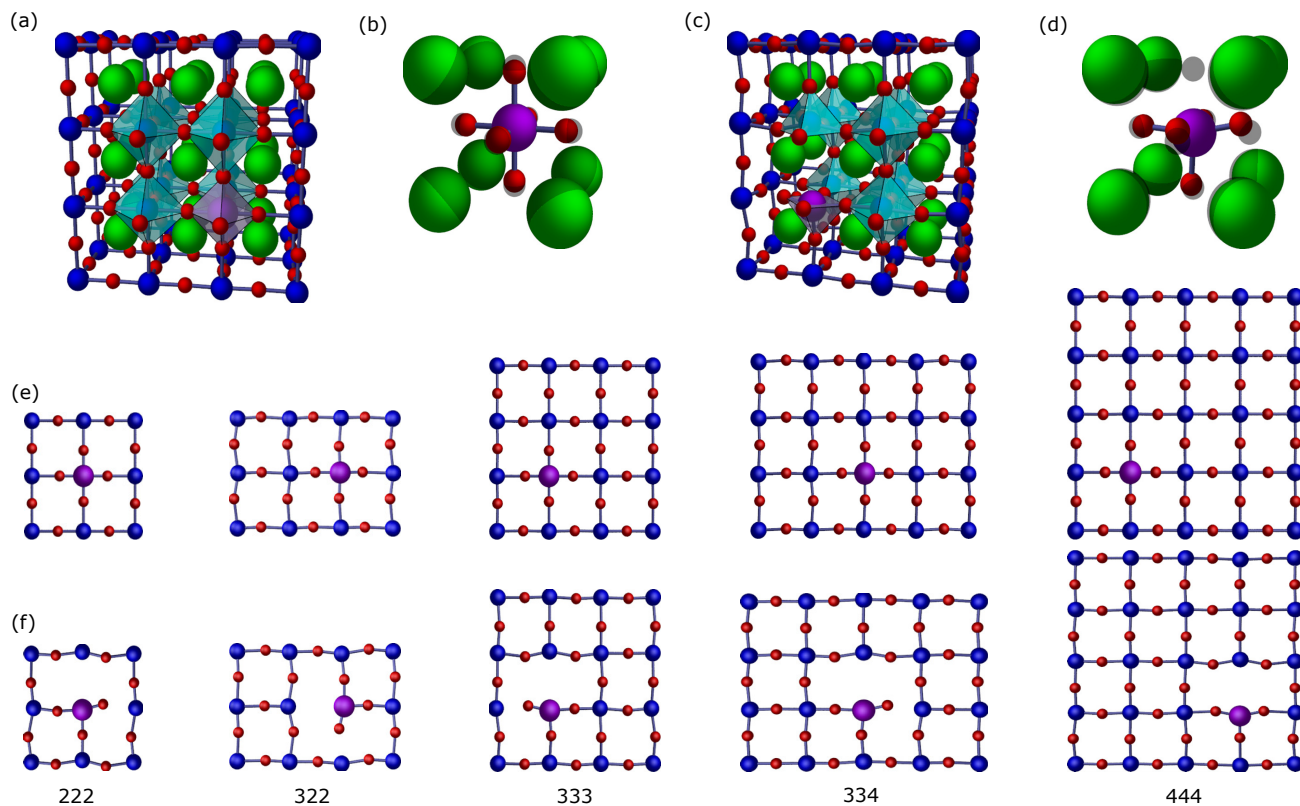
Figu 11 Cutaway of $3 \times 3 \times 3$ Mn_{Ti} (a) and $Mn_{Ti}-V_O$ (c) supercells with defect surrounding TiO_6 octahedra. Enlarged Mn_{Ti} B-cell (b) and enlarged $Mn_{Ti}-V_O$ B-cell (d) from $3 \times 3 \times 3$ supercell with locations of atoms in the pure lattice shaded. Cubic lattice in the defect plane from the Mn_{Ti} (e) and $Mn_{Ti}-V_O$ (f) for each differently sized supercell. For asymmetric $3 \times 2 \times 2$ and $3 \times 3 \times 4$ supercells, only the x- oriented defect is shown. Color code: Sr = green, Ti = blue, O = red, Mn = purple.
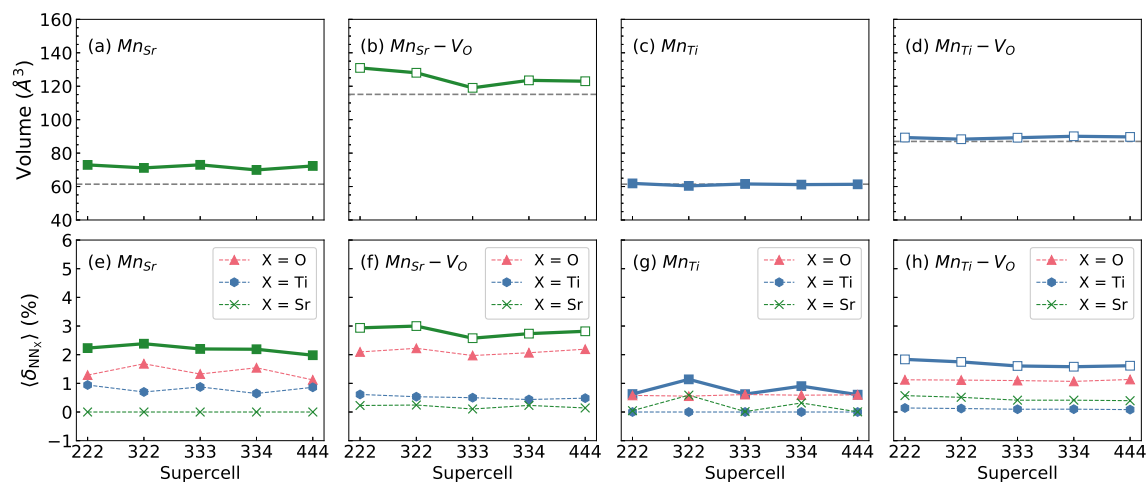
Figu 12 Defect Volumes (a-c) and Nearest Neighbor (d-f) displacements for doped supercells.
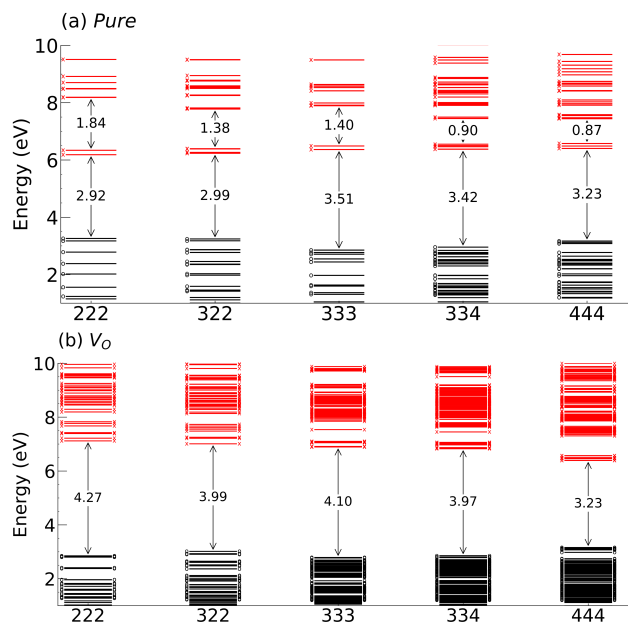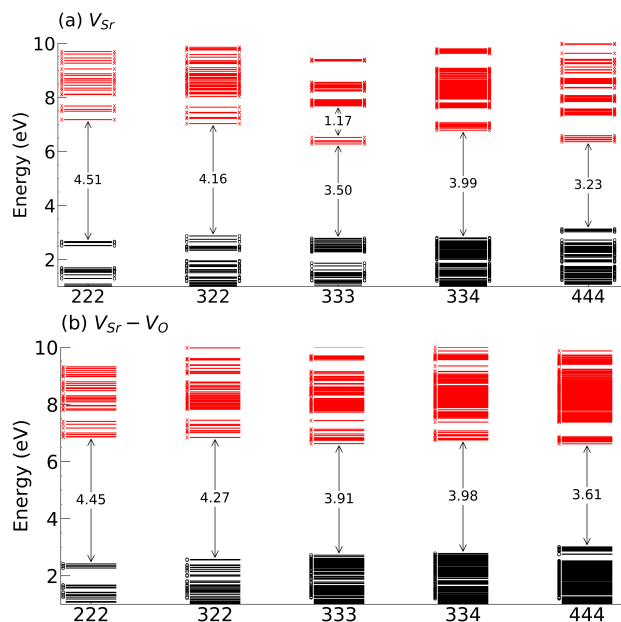
Figu 13 HSE06 predicted bands and charge densities at Γ for undefected (a) and V_O (b). Unoccupied orbitals are marked with red and with ×. Occupied orbitals are marked in black and with o. Only the x-orientation is plotted for asymmetric supercells.

Figu 14 HSE06 predicted bands and charge densities at Γ for V_{Sr} (a) and V_{Sr}–V_O (b). Unoccupied orbitals are marked with red and with ×. Occupied orbitals are marked in black and with o. Only the x-orientation is plotted for asymmetric supercells.

the orientation of the vacancy in the x- or z- direction for asymmetric supercells, with E_g for 3 x 2 x 2 V_{Ox} predicted to be 0.03 eV narrower than V_{Oz} (Fig. S12, ESI†). Notably, we do not observe any intra-bandgap states for V_O in any supercell that was reported by previous researchers.

3.6 Electronic Structure of A-Site defects

V_{Sr} also reveals large E_g widening that converges towards the bulk value in the largest supercells from 4.51 eV in 2 x 2 x 2 to 3.23 eV in 4 x 4 x 4. In both the HSE06 (Fig. 14a) calculated energy levels and full BLYP (Fig. S13, ESI†) band structures, the 3 x 3 x 4 supercell predicts and unusually large E_g, indicating that supercell symmetry is just as important in predicting electronic structure as size.

The corresponding double defect V_{Sr}–V_O causes little perturbation to the electronic structure, with the exception of 3 x 3 x 3 and 4 x 4 x 4 supercells. E_g in these supercells no longer approaches bulk value in both the BLYP (Fig. S13, ESI†) and HSE06 (Fig. 14b) calculations. Interestingly, E_g in the asymmetric 3 x 2 x 2 supercells is sensitive to orientation of the defect with a difference in E_g of approximately 0.35 eV between V_{Sr}–V_{Ox} and V_{Sr}–V_{Oz} in the HSE06 predicted energy levels. This also may be a consequence of the Γ-only sampling in these calculations, in which Γ differs between an occupied and vacant O site depending on the x- or z- orientation of the defect. The significant loss of curvature in the 2 x 2 x 2 and 3 x 2 x 2 full BLYP band structures is indicative of the high structural distortion in these supercells, indicating a greater contribution from localized orbitals, opposed to the highly delocalized bands of supercells 3 x 3 x 3 and larger. The reduced atomic density in the small doubly-defected supercells may also help justify E_g widening.

Doping with the Mn ion has potential to create intra-bandgap defect states localized on the dopant atom, indicated in the full BLYP band structures as very flat bands, and confirmed by analysis of the HSE06 charge densities. In addition to potentially narrowing E_g, these localized orbitals can potentially act as trap states for excited charge carriers, as well as recombination centers. Considering the two different defect site geometries calculated for Mn_{Sr} (Fig. 9), it is intuitive to expect two different electronic structures that correspond to the 4-coordinate face-centered Mn complex of the asymmetric 3 x 2 x 2 and 3 x 3 x 4 supercells, and the 3-coordinate Mn complex of the cubic supercells. In the BLYP calculated band structures (Fig. S17, ESI†), this is the case with the 3-coordinate complex resulting in an occupied defect band located in the middle of the band gap, and the 4-coordinate face centered Mn-complex predicted by the asymmetric supercells showing as a deeper defect state just above VB edge, with possible additional defect states comprising the edge of the CB coinciding with the fermi level (E_F).

The presence of these defect states is confirmed in the HSE06 calculations. In both defect geometries, VBM is a singly occupied band located approximately 1 eV over the other occupied bands, and is localized on the dopant atom with t_{2g} character (② in Fig. 15a). In each geometry, there are three additional unoccupied Mn-localized orbitals, however with differing degeneracies. In the 3-coordinate Mn geometries, there is a non-degenerate deep defect state located approximately 1.5 eV below CBM. CBM in these geometries consist of two degenerate orbitals with charge density shared between Mn atom and nearby atoms (③ in Fig. 15a). Furthermore, exclusively the 2 x 2 x 2 supercell predicts an additional defect state with primarily d_{z^2} character (① in Fig. 15a), centered on the Ti atom nearest the dopant. In the face-
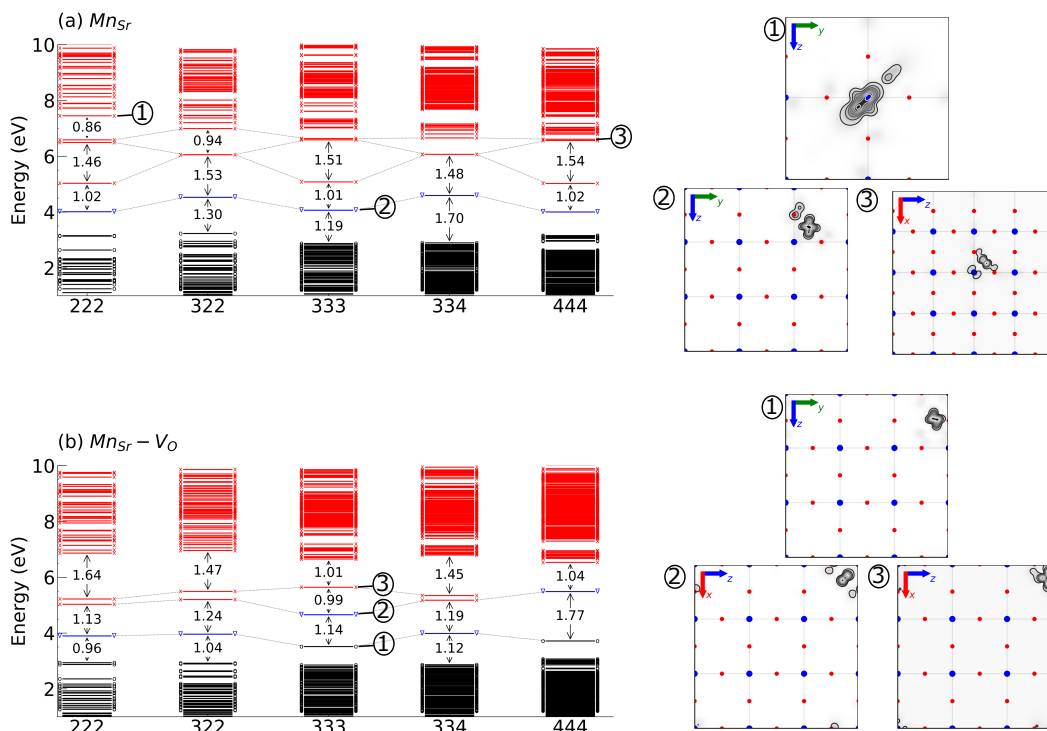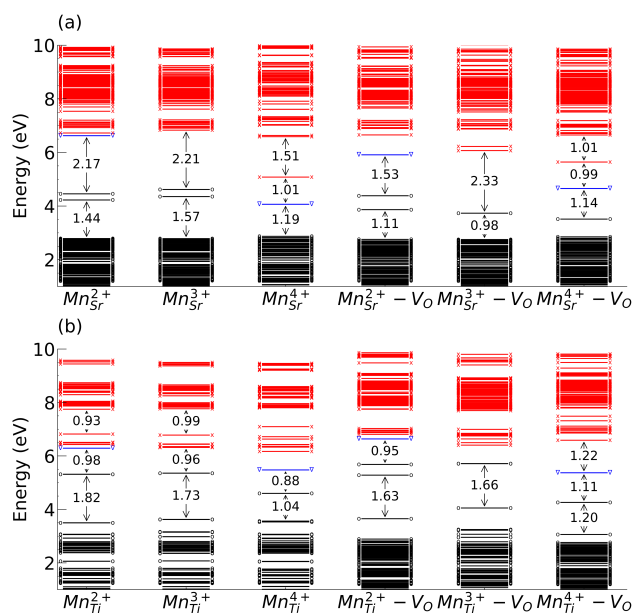
Figu 15 HSE06 predicted bands and charge densities at Γ for Mn_{Sr} (a) and $Mn_{Sr}-V_O$ (b). Unoccupied orbitals are marked with red and with x. Singly occupied orbitals are marked with blue and with ∇. Occupied orbitals are marked in black and with o. Gray lines trace the locations of localized orbitals with similar character. Only the x-orientation is plotted for asymmetric supercells. Charge density is summed along the perpendicular axis and indicated by shading and contour lines. The blue and red dots are a visual guide to indicate Ti and O lattice positions in the undefected supercell and do not represent the exact locations of atoms in the relaxed supercell.

centered 4-coordinate geometries, the two degenerate localized orbitals comprise a shallower defect state, approximately 0.94 eV or less below CBM. CBM in these geometries is a single localized orbital.

Considering the similar square planar geometry between the face-centered Mn_{Sr} geometries, and the 4-coordinate square planar $Mn_{Sr}-V_O$ defect complexes predicted by 2 x 2 x 2, 3 x 2 x 2, and 3 x 3 x 4, it is unsurprising that the latter also predicts 3 total localized orbitals in the vicinity of the bandgap (Fig. 15b). However, all mid-gap states are much further (> 1 eV) below CB. There is little dependence on the orientation of the defect in asymmetric 3 x 2 x 2 and 3 x 3 x 4 supercells. The 5-coordinate $Mn_{Sr}-V_O$ geometries of 3 x 3 x 3 and 4 x 4 x 4 predict critically different electronic structures. 3 x 3 x 3 continues to predict three localized orbitals, but the lowest of these is occupied in the VB (① in Fig. 15b). The 4 x 4 x 4 supercell also possess an occupied localized orbital, and the singly occupied Mn-localized VBM 1.77 eV above the remainder of the VB, and 1.04 eV below the CBM. Notably, 4 x 4 x 4 only predicts these two localized orbitals in the vicinity of the band gap, opposed to three localized states predicted by all other supercells. Combined ultraviolet photoelectron spectroscopy (UPS), inverse photoemission spectroscopy (IPES), and XPS spectra could provide relative energies of VB, CB, and Mn states that would allow some of these electronic structure to be ruled-out (or favored).

Doping with $Mn^{2+/3+}$ creates additional electronic structures (Fig. 16a & S14, ESI†). In the five coordinate Mn complex pre-

Figu 16 HSE06 predicted bands and charge densities at Γ in 3 x 3 x 3 supercell for $Mn^{2+/3+/4+}$ at the a-site (a) and b-site(b). Unoccupied orbitals are marked with red and with x. Singly occupied orbitals are marked with blue and with ∇. Occupied orbitals are marked in black and with o.
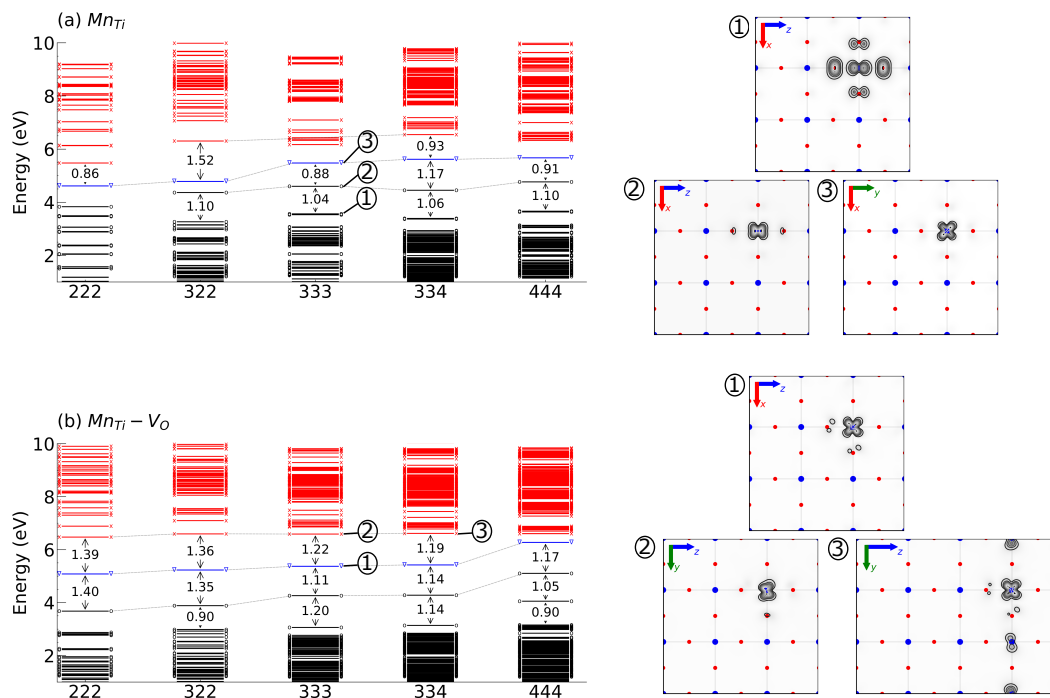
Figu   17 HSE06 predicted bands and charge densities at Γ for Mn_{Ti} (a) and Mn_{Ti}–V_O (b). Unoccupied orbitals are marked with red and with x. Singly occupied orbitals are marked with blue and with ∇. Occupied orbitals are marked in black and with o. Gray lines trace the locations of localized orbitals with similar character. Only the x-orientation is plotted for asymmetric supercells. Charge density is summed along the perpendicular axis and indicated by shading and contour lines. The blue and red dots are a visual guide to indicate Ti and O lattice positions in the undefected supercell and do not represent the exact locations of atoms in the relaxed supercell.

dicted by both by Mn_{Sr}^{2+} and Mn_{Sr}^{3+} (Fig. S9, ESI†), there are two electronic states located approximately 1.5 eV above the remainder of the VB with splitting of approximately 0.1 eV. The higher of these orbitals is localized on the dopant, and constitutes VBM in Mn_{Sr}^{3+}, whereas the additional electron of Mn_{Sr}^{2+} singly occupies a delocalized orbital with Ti t_{2g} character, which is isoelectronic with the bottom of CB. The Mn_{Sr}^{3+}–V_O predicts a similar 5-coordinate geometry as the 2 x 2 x 2, 3 x 2 x 2, and 3 x 3 x 4 Mn_{Sr}^{4+}–V_O supercells, and the electronic structure is generally the same with the extra electron contributed by Mn^{3+} filling the previously singly occupied VB. Mn_{Sr}^{2+}–V_O also predicts a similar geometry, however the electronic structure is significantly different. In contrast to the other A-site defects, 4 localized states are predicted. In addition to those three with Mn t_{2g} character common in the other defects, the lowest of these occupied intrabandgap states located 1.11 eV above the rest of the VB has significant hybridization with with the nearby Ti d_{z^2} orbitals forming an F-center between the two adjacent Ti atoms.

3.7 Electronic Structure of B-Site defects

Single and double vacancies on the B-site generally also lead to large E_g (Fig. S15, ESI†), like the A-site vacancies. Specifically, the V_{Ti} results in maximum E_g widening to 4.61 eV in the 2 x 2 x 2 and converges to the bulk value by the 4 x 4 x 4 supercell, with the biggest jump in convergence between 3 x 2 x 2 and 3 x 3 x 3 of approximately 0.78 eV in the HSE06 predicted structures. Full BLYP band structures (Fig. S16, ESI†) also predict E_g widening in smallest supercells to 2.88 eV and 2.51 eV in 2 x 2 x 2 and

3 x 2 x 2 supercells, but full convergence to bulk value by the 3 x 3 x 3 supercell. The larger V_{Ti}–V_O defect results in smaller E_g widening to a HSE06 predicted maximum of 4.14 eV in the 2 x 2 x 2 supercell. However, this value is slower to converge, remaining fairly constant between 3.9 and 4.0 eV in all supercells, until only reaching the bulk value at the 4 x 4 x 4 in both BLYP and HSE06 calculations (Fig. S15, ESI†). Unexpectedly, both functionals calculate the 3 x 3 x 3 supercell to have a larger E_g than its asymmetric neighbors.

The Mn_{Ti} defect shows high sensitivity to supercell size. The smallest E_g occurs for the 2 x 2 x 2 supercell, predicting metallic behavior with ΔE = 0.86 eV between the between the singly occupied VBM and CBM. This feature is unique to the HSE06 predicted bands with the full BLYP band structures (Fig. S16, ESI†) indicating E_g=1.53 eV, yet E_F is localized in the CB. Analysis of the charge density indicates that the singly occupied VBM and next highest band are located entirely on the Mn ion (② and ③ in Fig. 17a). The CBM largely retains this character, albeit with significant O $2p$ contributions. Only in the asymmetric supercells is CBM is completely localized on Mn with t_{2g} character. In supercells 3 x 3 x 3 and larger, there is the appearance of an additional localized state not centered on the Mn ion, but rather on the O $2p$ orbitals surrounding the dopant (① in Fig. 17a). This state occurs for several bands immediately below the singly occupied VBM, and cannot occur in supercells 3 x 3 x 3 or smaller due to the majority of atoms in small supercells being defect adjacent. The 3 x 2 x 2 and 3 x 3 x 4 supercells both predict larger E_g, consistent with the increased Ti-O bond lengths for asymmetric

supercells (Fig. 1d) and thus poorer orbital overlap. The full BLYP bandstructures also produce highly variable results. In each case, E_g is decreased from the bulk value, and E_F is localized in the CB.

Doping with $Mn^{2+/3+}$ causes minimal change in the predicted geometry of each Mn_{Ti} supercell, however varying electronic structures are predicted (Fig. 16b). The HSE06 calculations predict that VBM in Mn_{Ti}^{3+} becomes two doubly occupied bands degenerate at Γ. Both of these states have Mn t_{2g}-like character, and one of them shares significant charge density with the surrounding O $2p$ orbitals. These are approximately 1.73 eV higher than the remainder of VB, and 0.96 eV below the conduction band edge. This band alignment is nearly identical in the Mn_{Ti}^{2+} defect, with the extra electron residing in the delocalized CBM with Ti t_{2g} character. The BLYP predicted band structures do not capture these subtle changes, and deviation from the 3 x 3 x 3 Mn_{Ti}^{4+} band structure is marginal (Fig. S14, ESI†).

In Mn_{Ti}–V_O supercells, most supercells retain three localized Mn orbitals (① and ② in Fig. 15b), comprising VBM, CBM, and a singly occupied mid-gap state. However, as supercell size is increased, the localized orbital comprising CBM begins to delocalize among the nearby Ti atoms in plane with the dopant (③ in Fig. 17b), and is completely delocalized by the 4 x 4 x 4 supercell. Surprisingly, there is a significant difference in the electronic structures between the 3 x 3 x 4 Mn_{Ti}-V_{Ox} and 3 x 3 x 4 Mn_{Ti}-V_{Oz} supercells (Fig. S17, ESI†) with the location of the singly-occupied VBM. Although the same character is retained in both cases, the singly occpuied VBM of Mn_{Ti}-V_{Oz} is blueshifted to the CBM compared to the mid-gap location of Mn_{Ti}-V_{Ox}.

The full BLYP bandstructures (Fig. S16, ESI†) are generally consistent across all supercells, and align well with the HSE06 structures. Notably, both methods predict a significantly large E_g compared with Mn_{Ti}. Doping with Mn^{3+} produces two degenerate doubly occupied VBM (Fig. 16b) approximately 1.66 eV above the remainder of the valence band and 0.6 eV below CBM. Both of these states are localized on the Mn dopant. In the Mn_{Ti}^{2+}-V_O, the degeneracy of these two states is broken and they are separated by approximately 0.2 eV. The extra electron resides at the bottom of CB in a singly occupied localized Mn orbital. For the $Mn^{2+/3+}$ defects, the full BLYP bandstructures do not produce significant differences (Fig. S14, ESI†), other than slightly different E_g of 1.84 eV and 2.01 eV for Mn^{3+} and Mn^{2+} respectively.

4 Conclusion

We performed the first comprehensive study of the profound impact of supercell size and model parameters on calculated properties of $SrTiO_3$ point defects. Our analysis of cell-wide geometry and energetics suggest that the 3 x 3 x 3 supercell represents the greatest compromise between computational cost and minimization of computational artifacts. In general, all single and double vacancies widen the band gap and Mn dopants result in narrower band gaps or singly occupied defect states in the undoped gap.

However, a more detailed exploration of defect site geometries and electronic structure reveals high variability and differing properties even among the largest supercells studied here, demonstrating the importance of such benchmarking studies or

exploration of a variety of structures for each defect. While targeted experiments to determine the structure (PDF) and electronic structure (XPS, UPS, IEPS) of a typical Mn dopant would help add to the understanding of Mn-doped $SrTiO_3$, methods that can identify the lowest energy geometries irrespective of supercell size would limit the computational cost to such studies. Ultimately, our results indicate that for now both supercell size and shape should be explored to capture the range of substitution dopants and vacancies when the atoms have more degrees of freedom (like the V_{Sr}, Mn_{Sr}, Mn_{Sr}–V_O).

Furthermore, our calculations using Mn^{2+} and Mn^{3+} suggest the need to explore model parameter space in additional dimensions in order to gain a complete understand of the complex chemistry of Mn-doped $SrTiO_3$. Importantly the interesting gap states predicted for the Mn_{Sr}^{4+} and Mn_{Sr}^{4+}–V_O suggest that Mn_{Sr}^{4+} as opposed to Mn_{Sr}^{2+} doped structure should have interesting functionality.

Conflicts of interest

There are no conflicts to declare.

Acknowledgements

Notes and references

1 M. S. Wrighton, A. B. Ellis, P. T. Wolczanski, D. L. Morse, H. B. Abrahamson and D. S. Ginley, *Journal of the American Chemical Society*, 1976, **98**, 2774–2779.

2 K. Domen, S. Naito, M. Soma, T. Onishi and K. Tamaru, *Journal of the Chemical Society, Chemical Communications*, 1980, 543–544.

3 D. I. Bilc, C. G. Floare, L. P. Zârbo, S. Garabagiu, S. Lemal and P. Ghosez, *Journal of Physical Chemistry C*, 2016, **120**, 25678–25688.

4 P. Noël, F. Trier, L. M. Vicente Arche, J. Bréhin, D. C. Vaz, V. Garcia, S. Fusil, A. Barthélémy, L. Vila, M. Bibes and J. P. Attané, *Nature*, 2020, **580**, 483–486.

5 C. Baeumer, C. Schmitz, A. H. Ramadan, H. Du, K. Skaja, V. Feyer, P. Muller, B. Arndt, C. L. Jia, J. Mayer, R. A. De Souza, C. Michael Schneider, R. Waser and R. Dittmann, *Nature Communications*, 2015, **6**, 6:8610.

6 A. V. Kovalevsky, M. H. Aguirre, S. Populoh, S. G. Patrício, N. M. Ferreira, S. M. Mikhalev, D. P. Fagg, A. Weidenkaff and J. R. Frade, *Journal of Materials Chemistry A*, 2017, **5**, 3909–3922.

7 C. Ricca, I. Timrov, M. Cococcioni, N. Marzari and U. Aschauer, *arXiv*, 2020, **2**, 23313.

8 A. Marthinsen, T. Grande and S. M. Selbach, *The Journal of Physical Chemistry C*, 2020, **124**, 12922–12932.

9 X. L. Dong, K. H. Zhang and M. X. Xu, *Frontiers of Physics*, 2018, **13**, 1–7.

10 P. Sikam, P. Moontragoon, C. Sararat, A. Karaphun, E. Swat-sitang, S. Pinitsoontorn and P. Thongbai, *Applied Surface Science*, 2018, **446**, 92–113.

11 T. Shen, C. Hu, H. L. Dai, W. L. Yang, H. C. Liu, C. L. Tan and X. L. Wei, *Optik*, 2016, **127**, 3055–3058.

12 O. E. Kvyatkovskii, *Physics of the Solid State*, 2012, **54**, 1397–1407.

13 L. Zhang, B. Liu, H. Zhuang, P. R. Kent, V. R. Cooper, P. Ganesh and H. Xu, *Computational Materials Science*, 2016, **118**, 309–315.

14 D. Kan, T. Terashima, R. Kanda, A. Masuno, K. Tanaka, S. Chu, H. Kan, A. Ishizumi, Y. Kanemitsu, Y. Shimakawa and M. Takano, *Nature Materials*, 2005, **4**, 816–819.

15 M. Choi, F. Oba, Y. Kumagai and I. Tanaka, *Advanced Materials*, 2013, **25**, 86–90.

16 J. P. Buban, H. Iddir and S. Öğüt, *Physical Review B - Condensed Matter and Materials Physics*, 2004, **69**, 3–6.

17 A. Janotti, J. B. Varley, M. Choi and C. G. Van De Walle, *Physical Review B - Condensed Matter and Materials Physics*, 2014, **90**, 1–6.

18 C. Mitra, C. Lin, J. Robertson and A. A. Demkov, *Physical Review B - Condensed Matter and Materials Physics*, 2012, **86**, 1–8.

19 R. Evarestov, E. Kotomin and Y. F. Zhukovskii, *International Journal of Quantum Chemistryonal Journal*, 2005, **106**, 2173–2183.

20 C. Freysoldt, B. Grabowski, T. Hickel, J. Neugebauer, G. Kresse, A. Janotti and C. G. Van De Walle, *Reviews of Modern Physics*, 2014, **86**, 253–305.

21 S. Y. Chung, D. Y. Yoon and S. J. L. Kang, *Acta Materialia*, 2002, **50**, 3361–3371.

22 U. N. Gries, M. Kessel, F. V. Hensling, R. Dittmann, M. Martin and R. A. De Souza, *Physical Review Materials*, 2020, **4**, 41–46.

23 J. N. Baker, P. C. Bowes, J. S. Harris and D. L. Irving, *Journal of Applied Physics*, 2018, **124**, 122903.

24 R. A. Mackie, S. Singh, J. Laverock, S. B. Dugdale and D. J. Keeble, *Physical Review B - Condensed Matter and Materials Physics*, 2009, **79**, 1–8.

25 D. J. Keeble, S. Wicklein, R. Dittmann, L. Ravelli, R. A. MacKie and W. Egger, *Physical Review Letters*, 2010, **105**, 3–6.

26 R. A. Maier, T. A. Pomorski, P. M. Lenahan and C. A. Randall, *Journal of Applied Physics*, 2015, **118**, 164102.

27 R. A. Maier and C. A. Randall, *Journal of the American Ceramic Society*, 2016, **99**, 3350–3359.

28 R. A. Maier, A. C. Johnston-Peck and M. P. Donohue, *Advanced Functional Materials*, 2016, **26**, 8325–8333.

29 I. Fongkaew, J. T-Thienprasert and S. Limpijumnong, *Ceramics International*, 2017, **43**, S381–S385.

30 H. Mansoor, W. L. Harrigan, K. A. Lehuta and K. R. Kittilstved, *Frontiers in Chemistry*, 2019, **7**, 1–8.

31 R. A. Maier, E. Cockayne, M. Donohue, G. Cibin and I. Levin, *Chemistry of Materials*, 2020, **32**, 4651–4662.

32 P. Giannozzi, S. Baroni, N. Bonini, M. Calandra, R. Car, C. Cavazzoni, D. Ceresoli, G. L. Chiarotti, M. Cococcioni, I. Dabo, A. Dal Corso, S. De Gironcoli, S. Fabris, G. Fratesi, R. Gebauer, U. Gerstmann, C. Gougoussis, A. Kokalj, M. Lazzeri, L. Martin-Samos, N. Marzari, F. Mauri, R. Mazzarello, S. Paolini, A. Pasquarello, L. Paulatto, C. Sbraccia, S. Scandolo, G. Sclauzero, A. P. Seitsonen, A. Smogunov, P. Umari and R. M. Wentzcovitch, *Journal of Physics Condensed Matter*, 2009, **21**, 395502.

33 P. Giannozzi, O. Baseggio, P. Bonfà, D. Brunato, R. Car, I. Carnimeo, C. Cavazzoni, S. De Gironcoli, P. Delugas, F. Ferrari Ruffino, A. Ferretti, N. Marzari, I. Timrov, A. Urru and S. Baroni, *Journal of Chemical Physics*, 2020, **152**, 154105.

34 A. D. Becke, *Physical Review A*, 1988, **38**, 3098–3100.

35 C. Lee, Y. Weitao and R. Parr, *Physical Review B*, 1988, **37**, 785–789.

36 S. Piskunov, E. Heifets, R. Eglitis and B. G., *Compuational Materials Science*, 2004, **29**, 165–178.

37 E. Holmström, P. Spijker and A. S. Foster, *Proceedings of the Royal Society A: Mathematical, Physical and Engineering Sciences*, 2016, **472**, 20160293.

38 G. Kresse and J. Hafner, *Physical Review B*, 1993, **47**, 558–561.

39 G. Kresse and J. Furthmüller, *Computational Materials Science*, 1996, **6**, 15–50.

40 G. Kresse and J. Furthmüller, *Physical Review B*, 1996, **54**, 11169–11186.

41 J. Heyd, G. E. Scuseria and M. Ernzerhof, *Journal of Chemical Physics*, 2003, **118**, 8207–8215.

42 A. V. Krukau, O. A. Vydrov, A. F. Izmaylov and G. E. Scuseria, *Journal of Chemical Physics*, 2006, **125**, 224106.

43 W. P., *Acta Crystallographica Section B: Structural Science*, 1997, **53**, 32–43.

44 W. Jauch and A. Palmer, *Physical Review B - Condensed Matter and Materials Physics*, 1999, **60**, 2961–2963.

45 B. I., *Journal of Physics: Conference Series*, 2017, **833**, 012001.

46 H. Sakai, J. Fujioka, T. Fukuda, D. Okuyama, D. Hashizume, F. Kagawa, H. Nakao, Y. Murakami, T. Arima, A. Q. Baron, Y. Taguchi and Y. Tokura, *Physical Review Letters*, 2011, **107**, 1–5.

47 V. V. Laguta, I. V. Kondakova, I. P. Bykov, M. D. Glinchuk, A. Tkach, P. M. Vilarinho and L. Jastrabik, *Physical Review B - Condensed Matter and Materials Physics*, 2007, **76**, 2–7.

48 N. E. Brese and M. O'Keeffe, *Acta Crystallographica Section B*, 1991, **47**, 192–197.

49 K. Van Benthem, C. Elsässer and R. H. French, *Journal of Applied Physics*, 2001, **90**, 6156–6164.